Journal of Zhejiang University-SCIENCE A (Applied Physics & Engineering) 2023 24(10):859-874
www.jzus.zju.edu.cn; www.springer.com/journal/11582
E-mail: jzus_a@zju.edu.cn

Research Article

https://doi.org/10.1631/jzus.A2300087

Microfluidic fuel cells integrating slanted groove micro-mixers to terminate growth of depletion boundary layer thickness

Jinchi SUN[1], Xiongwei TIAN[1], Zhangqing LIU[1], Jie SUN[2], Menglian ZHENG[1,3]✉

[1]*Institute of Thermal Science and Power Systems, College of Energy Engineering, Zhejiang University, Hangzhou 310027, China*
[2]*Institute of Energy and Environment Engineering, NingboTech University, Ningbo 315100, China*
[3]*State Key Laboratory of Clean Energy Utilization, Hangzhou 310027, China*

Abstract: Because of potential high energy densities, microfluidic fuel cells can serve as micro-scale power sources. Because microfluidic fuel cells typically operate in the co-laminar flow regime to enable a membrane-less design, they generally suffer from severe mass transfer limitations with respect to diffusion transport. To address this issue, a novel channel design that integrates slanted groove micro-mixers on the side walls of the channel is proposed. Numerical modeling on the design of groove micro-mixers and grooveless design demonstrates a mass transfer enhancement that has a 115% higher limiting current density and well-controlled convective mixing between the oxidant and the fuel streams with the use of slanted groove micro-mixers. Moreover, the growth of the thickness of the depletion boundary layer is found to be terminated within approximately 2 mm from the channel entrance, which is distinct from the constantly growing pattern in the grooveless design. In addition, a simplified mass transfer model capable of modeling the mass transfer prFocess with the presence of the transverse secondary flow is developed. Further, a dimensionless correlation is derived to analyze the effects of the design parameters on the limiting current density. The present theoretical study paves the way towards an optimal design of a microfluidic fuel cell integrating groove micro-mixers.

Key words: Microfluidic; Fuel cell; Membraneless; Slanted groove micro-mixer; Mass transfer; Depletion boundary layer

1 Introduction

Over the past few decades, studies on micro-scale power sources with high power densities and extended charging/discharging durations have been motivated by social demands for portable devices, such as cell phones, laptops, and portable instruments for diagnostics and field-trip analysis (Kundu et al., 2007; Moreno-Zuria et al., 2017; Gurrola et al., 2021). While the development of traditional batteries is thought to be unlikely to meet the growing power requirement of portable devices, micro fuel cells have become a promising substitute power source owing to their high energy densities and ease of recharge by refilling fuels (Dyer, 2002; Modestino et al., 2016).

The miniaturization of conventional fuel cells by an approach based on micro-electromechanical systems has led to several types of membrane-based micro fuel cells, such as micro proton exchange membrane fuel cells and micro direct methanol fuel cells (Nguyen and Chan, 2006). More recent studies have demonstrated that the laminarity of the flow at the micro scale can be exploited to develop membrane-less micro fuel cells, which are also called microfluidic fuel cell (Ferrigno et al., 2002; Cohen et al., 2005a, 2005b). In a typical microfluidic fuel cell, the electrolytes (the oxidant stream and the fuel stream) flow side-by-side down a single channel and mixing between the electrolytes occurs by diffusion alone (Kjeang et al., 2009). The exclusion of the proton exchange membrane enables the elimination of the membrane fouling or damage issue (Ferrigno et al., 2002), better water management (Choban et al., 2005b), reduced system cost (Tsuchiya and Kobayashi, 2004), and simplified fabrication of the micro fuel cell (Ferrigno et al., 2002).

Since the invention of microfluidic fuel cells by Ferrigno et al. (2002), various types of fuels and oxidants (Ferrigno et al., 2002; Choban et al., 2004, 2005a,

✉ Menglian ZHENG, menglian_zheng@zju.edu.cn
Menglian ZHENG, https://orcid.org/0000-0002-4418-4361

Received Feb. 15, 2023; Revision accepted May 15, 2023;
Crosschecked Sept. 14, 2023

2005b; Hasegawa et al., 2005; Lee et al., 2007; Brushett et al., 2009), supporting electrolytes (Choban et al., 2005a, 2005b; Jayashree et al., 2006; Brushett et al., 2009), and electrode materials (Kjeang et al., 2007c; Lee and Kjeang, 2013) have been investigated to improve their performance. The power density of microfluidic fuel cells has been significantly improved to a figure that is comparable to that of micro direct methanol fuel cells (Shaegh et al., 2011). However, the high power densities reported in the literature have mostly been achieved at elevated flow rates at the cost of reduced fuel utilization efficiency (Jayashree et al., 2010). At relatively low flow rates, the power densities decrease drastically owing to the severe mass transfer limitations with respect to the diffusion transport (Ferrigno et al., 2002; Choban et al., 2004; Bazylak et al., 2005; Kjeang et al., 2007a; Ahmed et al., 2008; Shaegh et al., 2012). Therefore, in recent studies on microfluidic fuel cells, effective approaches for mass transfer enhancement have been stressed with the aim of achieving high power densities without significantly elevated flow rates (Nasharudin et al., 2014).

The air-breathing microfluidic fuel cell, in which a gas diffusion electrode was used as the cathode, was proposed by Jayashree et al. (2005) to address the mass transfer limitation at the cathode (Choban et al., 2005a; Chang et al., 2006) for microfluidic fuel cells using formic acid or methanol as the fuel and dissolved oxygen as the oxidant. With the oxygen delivered directly from the ambient air, four orders of magnitude higher diffusivity and more than doubled concentration of the oxygen were achieved, resulting in the peak power density being increased by more than four-fold (Jayashree et al., 2005). Later measurements confirmed that this air-breathing microfluidic fuel cell was no longer limited in mass transfer at the cathode (Jayashree et al., 2010). Further, microfluidic fuel cells using flow-through porous electrodes were pioneered by Kjeang et al. (2008) in which the fuel and oxidant streams were forced to flow through porous electrodes before merging and flowing side-by-side, thus enhancing the mass transfer of the reactants to the electrodes. Experiments with all-vanadium redox couples showed that the peak power density and fuel utilization nearly tripled and doubled, respectively, compared to the microfluidic fuel cell that used planar electrodes in the Reynolds number range of Re=2–20. The performance of this design, however, cannot be sustained at high current densities owing to increases in the ohmic losses (Kjeang et al., 2008; Lee and Kjeang, 2013). Shaegh et al. (2012) demonstrated that such a flow-through porous electrode can also be applied to air-breathing microfluidic fuel cells as the anode for mass transfer enhancement, though at the expense of increased pressure drops.

Alternatively, mass transfer enhancement in microfluidic fuel cells can be achieved by integrating groove micro-mixers. For example, the integration of slanted groove micro-mixers (SGMs) in a microfluidic fuel cell was pioneered by Yoon et al. (2006). Their experimental study of the microfluidic fuel cell with symmetrical herringbone ridges patterned along the bottom wall of the channel demonstrated a 10%–40% higher fuel utilization compared to a microfluidic fuel cell without ridges. The mass transfer enchantment was attributed to the continuous replacement of the depletion boundary layer with fresh solution from the bulk electrolyte, which was facilitated by the transverse secondary flow induced by the ridges (Yoon et al., 2006). Although beneficial to the mass transfer process, the presence of the transverse secondary flow can lead to convective mixing between the electrolytes (i.e., the oxidant and the fuel streams) and thus cause problems with operations owing to fuel crossover (when the mixing region overlaps with the electrode and a parasitic current is generated) (Xuan et al., 2011). To address the fuel crossover issue, optimized symmetrical herringbone ridges with an additional ridge along the centerline were proposed by Marschewski et al. (2015). By adding an extra ridge, convective mixing between the electrolytes was under control up to Re≈325, and the limiting current density was more than doubled compared to the microfluidic fuel cell without ridges in the range of Re= 155–470 (Marschewski et al., 2015). Integration of staggered herringbone mixers (SHMs) in microfluidic fuel cells has also been studied. Xuan et al. (2011) theoretically studied a microfluidic fuel cell with staggered herringbone ridges patterned along the bottom wall of the channel and demonstrated a mass transfer enhancement compared to that for microfluidic fuel cells without ridges. A counter-flow configuration was used to avoid convective mixing between the electrolytes but was at the expense of increased ohmic losses.

In addition to topographical patterning of the channel wall, the integration of groove micro-mixers in microfluidic fuel cells can also be implemented by using groove electrodes. For example, Ha and Ahn

(2014) reported that a 36.56% higher peak power density was achieved by using electrodes incorporating 0.1-μm-deep slanted grooves (Lee and Ahn, 2015). Only minor convective mixing occurred due to the weakness of the transverse secondary flow triggered by the grooves. The microfluidic fuel cell with 50-μm-deep grooves etched on the electrodes in the staggered-herringbone pattern was studied by da Mota et al. (2012). More than doubled peak power density and more than tripled limiting current density were achieved, with the electrolytes being separated by a non-selective porous plate to suppress convective mixing between the electrolytes.

To summarize, significant improvements in fuel utilization, limiting current density, and peak power density have been achieved by integrating groove micro-mixers in microfluidic fuel cells. However, few insights into the mass transfer process in microfluidic fuel cells that integrate groove micro-mixers have been gained even though the transverse secondary flow triggered by the groove micro-mixers has significant effects on the mass transfer process (Kirtland et al., 2009).

In the present study, a novel design of microfluidic fuel cells that integrates SGMs on the side walls of the channel is proposed and studied. By using a numerical model, the performance of the proposed microfluidic fuel cells is investigated in terms of the limiting current density and convective mixing between the electrolytes. In addition, the developing pattern of the depletion boundary layer along the channel is studied via a simplified mass transfer model approach to facilitate a deeper understanding of the mass transfer process of the reactants from the electrolyte to the electrode with the presence of the transverse secondary flow. Further, the effects of design parameters on the limiting current density are analyzed systematically using a dimensionless correlation derived from the simplified mass transfer model to achieve enhanced mass transfer.

2 Methods

2.1 Geometries of microfluidic fuel cells

As shown in Figs. 1a and 1b, in the microfluidic fuel cells proposed in the present study, SGMs are integrated on the two opposing side walls of the channel symmetrically with respect to the interface between

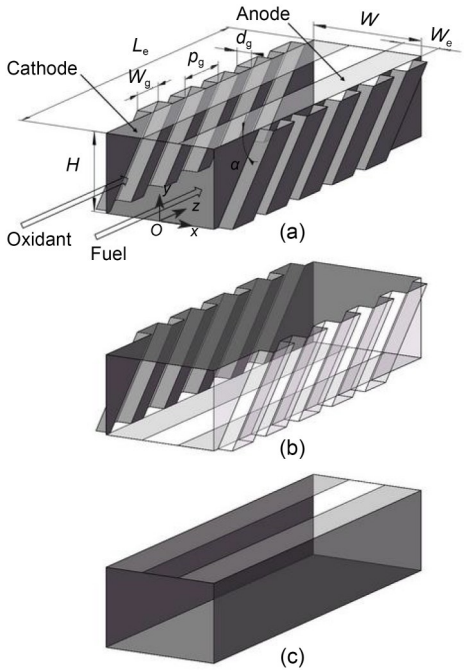

Fig. 1 Illustration of the geometries of the three microfluidic fuel cell designs of microfluidic fuel cells that integrate SGMs: (a) electrodes on the top wall, labeled as N1; (b) electrodes on the bottom wall, labeled as N2; (c) grooveless microfluidic fuel cell, labeled as N3

the electrolytes. A helical flow pattern is expected to be induced in each electrolyte stream by the grooves when the electrolytes flow through the channel (Stroock et al., 2002). Two positions of the electrodes, i.e., on the top wall and on the bottom wall, are considered and these two designs are labeled as N1 and N2, respectively. The geometric parameters of the channel are determined, based on our preliminary results, to illustrate the combined effects of the grooves on mass transfer enhancement and the mixing between the electrolytes. Specifically, the aspect ratio of the cross-section of the channel, i.e., W/H, is set as 1.5, and the width of the electrode (W_e) is set as half of the height of the channel (H), where H=200 μm. Referring to the guidelines for optimizing the helical flow in groove micro-mixers (Lynn and Dandy, 2007; Forbes and Kralj, 2012), the geometric parameters of the grooves are set as d_g/H=0.2, W_g/d_g=2.5, p_g/H=0.8, and α=45°, where d_g and W_g denote the depth and the width of grooves, respectively, p_g denotes the spacing between the centerlines of two neighboring grooves, and α denotes the tilt angle of grooves. The numbers of grooves are set to be 5, 10, 20, 40, and 80, with corresponding lengths of the electrode of L_e/H=5, 9, 17, 33, and 65, respectively, to

explore the effects of the length of the electrode. In addition, as shown in Fig. 1c, a grooveless microfluidic fuel cell labeled N3 is also studied for comparison; it has the same dimensions (H, W, W_e, and L_e) as the N1 and N2 designs.

2.2 Numerical model

In the present study, iron (II) sulfate (10 mol/m^3) in 1000-mol/m^3 sulfuric acid, and anthraquinone (5 mol/m^3) in 1000-mol/m^3 sulfuric acid are used as the fuel and oxidant, respectively. The reactions at the anode and cathode are shown in Eqs. (1) and (2), respectively:

$$Fe^{2+} \longrightarrow Fe^{3+} + e^-,\ E^0 = -0.77\ V, \quad (1)$$

$$AQ2S + 2H^+ + 2e^- \longrightarrow AQ2SH_2,\ E^0 = -0.09\ V, \quad (2)$$

where E^0 is the standard potential of the reaction, and AQ2S is the anthraquinone-2-sulphonate. To highlight the mass transfer enhancement by integrating SGMs, the operation of the microfluidic fuel cells in the mass transfer limited regime is modeled. Recognizing that the diffusion coefficient of the reactant in the fuel stream (Fe^{2+}, 1.0×10^{-10} m^2/s (Modestino et al., 2016)) is smaller than that of the reactant in the oxidant stream (AQ2S, 2.7×10^{-10} m^2/s (Modestino et al., 2016)), it is assumed that the limiting current density of the fuel cell is determined by mass transfer of reactant in the fuel stream, i.e., Fe^{2+}, which is modeled as follows.

First, the flow in the channel is modeled by the steady-state continuity equation and Navier-Stokes equation for incompressible flow with constant physical properties as:

$$\nabla \cdot \boldsymbol{v} = 0, \quad (3)$$

$$\rho \boldsymbol{v} \cdot \nabla \boldsymbol{v} = -\nabla p + \mu \nabla^2 \boldsymbol{v}, \quad (4)$$

where $\boldsymbol{v}$ is the velocity vector, ρ is the density of the electrolytes, μ is the dynamic viscosity of the electrolytes, and p is the pressure.

A Poiseuille flow with a specified average velocity U is imposed at the entrance of the channel, null velocity vector boundary conditions are used at the channel walls and the electrodes, and a zero gauge pressure condition is set at the exit of the channel.

A density of 1000-mol/m^3 sulfuric acid (ρ= 1059.5 kg/m^3 (Stroock et al., 2002)) is applied for both the fuel and oxidant streams because the concentration of the reactants is low. The dynamic viscosity of the electrolytes is set as the typical value for aqueous solutions at room temperature (μ=1.0×10^{-3} m/s^2).

The concentration distribution of Fe^{2+} is then obtained using the steady-state convective diffusion equation:

$$\boldsymbol{v} \cdot \nabla c - D\nabla^2 c = 0, \quad (5)$$

where c is the molar concentration of Fe^{2+}, and D (1×10^{-10} m^2/s (Marschewski et al., 2015)) is the diffusion coefficient of Fe^{2+}.

In the mass transfer limited regime, an instantaneous reaction of Fe^{2+} occurs at the anode (i.e., the concentration of Fe^{2+} at the anode surface c_s=0), and it is assumed that no reaction of Fe^{2+} occurs at the cathode and channel walls. Concentration of Fe^{2+} is set to c_0 (10 mol/m^3) at the inlet of the fuel stream and zero at the inlet of the oxidant stream.

With the concentration distribution of the reactant, the limiting current density can then be calculated:

$$J_{\lim} = \frac{n_e F}{L_e W_e} \int_0^{L_e} \int_0^{W_e} N(x, z)\, \mathrm{d}x\mathrm{d}z, \quad (6)$$

where n_e is the number of transferred electrons, F is the Faraday constant (equal to 96485 C/mol), and $N(x, z)=D(\partial c/\partial y)_s$ is the local flux of the reactant to the electrode calculated through Fick's law. Note that the subscript s is the short for the electrode surface.

The numerical calculation of the above equations is performed with the commercial computational fluid dynamics software ANSYS® Fluent 16.0, and structured meshes with an average size of 6 μm are generated in the software ANSYS® ICEM CFD 16.0. The meshes are further refined to an average size smaller than 1 μm near the anode to capture the concentration gradients there.

2.3 Simplified mass transfer model

To facilitate a deeper understanding of the mass transfer process in microfluidic fuel cells that integrate SGMs, a simplified mass transfer model is developed in the present study. The focus is placed on the mass transfer process within the depletion boundary layer of the fuel stream; the mass transfer processes in the bulk of the fuel and oxidant streams are out of the scope of this simplified model.

2.3.1 Assumptions

(1) The microfluidic fuel cell is mass transfer limited at the anode.

(2) The thickness of the depletion boundary layer is much smaller than the height of the channel (Nguyen and Chan, 2006).

(3) The impacts of mixing between the electrolytes are neglected.

(4) The effects of the depleted electrolytes going back to the electrode owing to the helical flow induced by the SGMs (Kirtland et al., 2006) are regarded as negligible.

(5) The velocity component parallel to the electrode can be approximated by the first term in Taylor's expansions of the distance from the electrode (i.e., the assumption of shear flow) (Newman, 1968).

(6) The diffusion transport parallel to the electrode due to minor concentration gradients is regarded as negligible.

2.3.2 Mathematical formulation

To make the problem explicitly solvable, the mass transfer domain is reduced to a series of 2D stream surfaces, which are vertical to the electrode under the assumption of shear flow. Thus, the mass transfer between each adjacent pair of the stream surfaces is considered to be negligible under Assumption 6. Consequently, the mass transfer process of the reactant from the electrolyte bulk to the electrode is modeled in individual stream surfaces.

According to the shear rate assumption and the steady-state continuity equation for incompressible flow, the velocity component along the s-axis (as defined in Fig. 2a), v_s, and the component along the y-axis, v_y, are formulated as follows:

$$v_s=\dot{\gamma}(s)\,y, \tag{7}$$

$$v_y=-\frac{1}{2}\dot{\gamma}'(s)\,y^2, \tag{8}$$

where $\dot{\gamma}(s)=(\partial v_s/\partial y)_{y=0}$ is the local velocity shear rate along the s-axis.

With the diffusion transport along the s-axis neglected under Assumption 6, the convective diffusion equation to be solved is:

$$v_s\frac{\partial c}{\partial s}+v_y\frac{\partial c}{\partial y}=D\frac{\partial^2 c}{\partial y^2}. \tag{9}$$

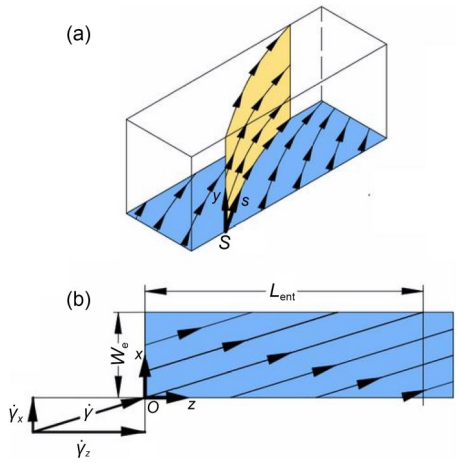

Fig. 2 Illustration of the coordinate systems used for the simplified mass transfer model: (a) semi-infinite region above the rectangular electrode surface (marked in blue), with the 2D coordinate system established in an arbitrary stream surface (marked in yellow) (curves with arrows illustrate the flow directions of the shear flow); (b) the special case where the velocity shear rate is constant over the electrode. The relation between the velocity shear rate along the *s*-axis and those along the *x*-axis and *z*-axis is shown. A 3D orthogonal coordinate system is established accordingly, with *y*-axis (not displayed) vertical to the electrode. L_{ent} is the entrance length. References to color refer to the online version of this figure

The boundary conditions are given by:

$$c=0, \quad \text{at } y=0, \tag{10}$$

$$c=c_0, \quad \text{at } s=0, \tag{11}$$

$$c\to c_0, \quad \text{at } y\to+\infty. \tag{12}$$

By solving the above equations, the concentration distribution of the reactant in the fuel stream (i.e., Fe^{2+}) is expressed as:

$$c=\frac{c_0}{\Gamma(4/3)}\int_0^{\xi}\exp(-t^3)\,\mathrm{d}t,$$

$$\xi=\frac{y\sqrt{\dot{\gamma}(s)}}{\left(9D\int_0^s\sqrt{\dot{\gamma}(\eta)}\,\mathrm{d}\eta\right)^{\frac{1}{3}}}, \qquad y>0,\ s>0, \tag{13}$$

where $\Gamma(4/3)=0.89298$, ξ denotes an intermediate variable, t is the integral variable between 0 and ξ, s is the specific spatial coordinate, and η is the integral variable between 0 and s.

Note that Eq. (13) is derived for an arbitrary stream surface and can be applied to the mass transfer process in a 3D domain.

2.3.3 Dimensionless correlation of limiting current density

Assuming that the velocity shear rate is constant over the electrode, Eq. (13) is rewritten in the 3D orthogonal coordinate system as shown in Fig. 2b:

$$c=\frac{c_0}{\Gamma(4/3)}\int_0^{\xi}\exp(-t^3)\,\mathrm{d}t,$$
$$\xi=\begin{cases} y\left(\dfrac{\dot{\gamma}_z}{9Dz}\right)^{\frac{1}{3}}, & \dfrac{z}{x}\leqslant\dfrac{\dot{\gamma}_z}{\dot{\gamma}_x},\\ y\left(\dfrac{\dot{\gamma}_x}{9Dx}\right)^{\frac{1}{3}}, & \dfrac{z}{x}>\dfrac{\dot{\gamma}_z}{\dot{\gamma}_x}, \end{cases} \tag{14}$$

where $\dot{\gamma}_z=(\partial v_z/\partial y)_{y=0}$ and $\dot{\gamma}_x=(\partial v_x/\partial y)_{y=0}$ are the velocity shear rate components along the z-axis and the x-axis, respectively.

The local flux of the reactant to the electrode can thus be obtained by using $N(x, z)=D(\partial c/\partial y)_{y=0}$. To express the local rate of the mass transfer to the electrode in a dimensionless form, the local Sherwood number is defined as:

$$Sh(x,z)=\frac{k(x,z)}{D/H}, \tag{15}$$

where $k(x, z)$ is the local mass transfer coefficient, which is defined as:

$$k(x,z)=\frac{N(x,z)}{c_0-c_s}, \tag{16}$$

where c_s is set as 0 considering an instantaneous reaction at the anode.

The average Sherwood number is then defined as:

$$Sh_{avg}=\frac{1}{L_eW_e}\iint Sh(x,z)\,\mathrm{d}x\mathrm{d}z. \tag{17}$$

By combining Eqs. (14)–(17), the expression of the average Sherwood number can be derived as:

$$Sh_{avg}=\frac{\sqrt[3]{3}/2}{\Gamma(4/3)}\left(\frac{\dot{\gamma}_zH^2}{D}\right)^{\frac{1}{3}}\left(\frac{L_e}{H}\right)^{-\frac{1}{3}}f(L_e^*), \tag{18}$$

where f is a dimensionless function defined as:

$$f(L_e^*)=\begin{cases}\dfrac{1}{5}L_e^*+1, & 0<L_e^*\leqslant 1,\\ \dfrac{1}{5}L_e^{*-\frac{2}{3}}+L_e^{*\frac{1}{3}}, & L_e^*>1,\end{cases} \tag{19}$$

and L_e^* is the dimensionless length of the electrode defined as:

$$L_e^*=\frac{L_e}{W_e\dot{\gamma}_z/\dot{\gamma}_x}. \tag{20}$$

By combining Eqs. (15)–(17) and the definition of the limiting current density given by Eq. (6), the relation between the limiting current density and the average Sherwood number is given by:

$$Sh_{avg}=\frac{J_{lim}}{n_eFc_0(D/H)}, \tag{21}$$

where J_{lim} denotes the limiting current density.

The dimensionless correlation of the limiting current density for the special case of the velocity shear rate being constant over the electrode is thus given by the expression of the average Sherwood number, i.e., Eq. (18).

Eq. (18) is then used to derive the dimensionless correlation of the limiting current density for the proposed microfluidic fuel cells that integrate SGMs. By treating the flow in the channel as the superposition of a uniaxial main flow and a much weaker secondary flow, the velocity shear rate component along the z-axis, $\dot{\gamma}_z$, is estimated according to the pressure-driven flow between two infinite parallel walls, which is given by (Kirtland et al., 2006):

$$\dot{\gamma}_z=\frac{6U}{H}, \tag{22}$$

where U denotes the average velocity of the electrolyte.

The dimensionless length of the electrode, L_e^*, is estimated based on its physical meaning. That is the length of the electrode non-dimensionalized by a characteristic length, $W_e\dot{\gamma}_z/\dot{\gamma}_x$. Referring to Fig. 2b, such a characteristic length is the distance along the channel that the shear flow travels during the process of passing by the electrode. Motivated by this observation, and assuming that the transverse secondary flow induced by the grooves varies periodically along the channel, the entrance length, L_{ent}, is defined as the average distance

along the channel that the shear flow travels during the process of passing by the electrode. Thus, L_e^* is estimated as:

$$L_e^* = \frac{L_e}{L_{ent}}. \tag{23}$$

The dimensionless correlation of the limiting current density for microfluidic fuel cells that integrate SGMs is then given by:

$$Sh_{avg} = 1.467 Pe^{\frac{1}{3}} \left(\frac{L_e}{H}\right)^{-\frac{1}{3}} f(L_e^*), \tag{24}$$

where $Pe=U/(D/H)$ is the Péclet number, $f(L_e^*)$ is given by Eq. (19), and the dimensionless length of the electrode L_e^* is given by Eq. (23). The limiting current density J_{lim} is related to the average Sherwood number Sh_{avg} according to Eq. (21). Regarding the expression of $f(L_e^*)$, the mathematical relationship between the average Sherwood number Sh_{avg} and length of the electrode L_e changes at the critical point of $L_e^*=L_e/L_{ent}=1$, which accounts for L_{ent} being referred to as 'the entrance length'.

3 Results and discussion

3.1 Model validation

3.1.1 Numerical model

The numerical modeling results of the limiting current density of microfluidic fuel cells at varying Reynolds number are compared against the experimental results in the previous study (Marschewski et al., 2017) to validate the credibility of the present numerical model, which is shown in Fig. 3. Results of a microfluidic fuel cell integrating SGMs on the bottom wall of the channel and a grooveless microfluidic fuel cell are presented. In general, the numerical model reproduces the scaling behavior at varying Reynolds numbers and the increase in the limiting current densities by integrating SGMs in the microfluidic fuel cell; however, it leads to lower limiting current density values than the experimental studies. While several factors neglected in the model may be responsible for the mismatch, it is suggested that the inaccuracy of parameters adopted in the model may be the dominant factor.

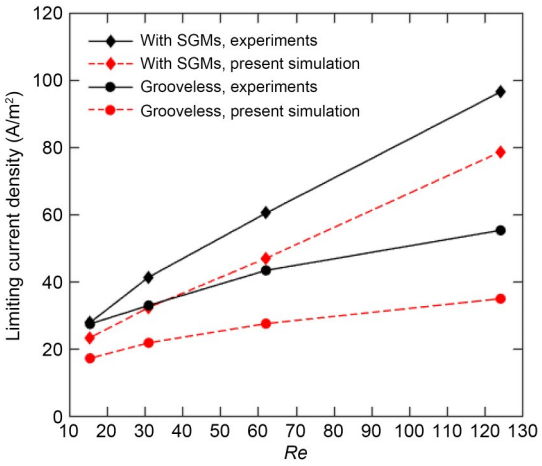

Fig. 3 Limiting current densities of microfluidic fuel cells at varying Reynolds numbers. The simulative results of the microfluidic fuel cells with and without SGMs are compared to the experimental results from Marschewski et al. (2017)

For example, the diffusion coefficient adopted in the model (1×10^{-10} m^2/s for Fe^{2+} (Marschewski et al., 2017)) may be lower than its actual value, leading to lower limiting current densities compared to the experimentally measured values. Further, in the experiments, mass transfer near the leading edge of the electrode may be enhanced by the transverse flow generated in the Y-shaped channel entrance, while this effect is neglected in the model by imposing a fully developed Poiseuille flow at the channel entrance.

A well-established formula for grooveless microfluidic fuel cells can be used to indirectly evaluate the diffusion coefficient based on the experimentally measured limiting current densities (Stroock et al., 2002):

$$J_{lim} = 1.467 n_e F c_0 D^{\frac{2}{3}} U^{\frac{1}{3}} L_e^{-\frac{1}{3}} H^{-\frac{1}{3}}. \tag{25}$$

The above calculation for the diffusion coefficient yields the average value $D=1.9\times10^{-10}$ m^2/s, which is sufficient to account for the mismatch shown in Fig. 3. Nevertheless, it should be noted that the following results have been presented in a dimensionless form and the inaccuracies and uncertainties in the parameters thus cause negligible effects on the validation of the conclusions here. Furthermore, these novel channel designs are regarded as general strategies for enhancing mass transfer of the microfluidic fuel cells, and the validation of the effectiveness of the proposed designs is not affected by inaccuracy and uncertainty in the diffusion coefficient.

3.1.2 Simplified mass transfer model

To validate the credibility of the developed simplified mass transfer model for investigating the mass transfer process within the depletion boundary layer, the predictions of local Sherwood number distributions in the proposed microfluidic fuel cells that integrate SGMs (N1 and N2 designs) are compared with the corresponding numerical results. The numerical modeling results of the velocity shear rate at the anode are used as the inputs of the simplified mass transfer model (Eq. (13)). In addition, the grooveless microfluidic fuel cell (N3 design) is also included, for which the theoretical values of the velocity shear rate of the Poiseuille flow in the rectangular channel (Kirtland et al., 2006) are used. As shown in Fig. 4, the simplified mass transfer model can capture the qualitative features of local Sherwood number distributions in the N1, N2, and N3 designs.

The dimensionless correlations of the limiting current density (Eq. (24)) obtained via the simplified mass transfer model are further validated by comparing the predictions of the limiting current density to those obtained using the numerical model for a variety of cases covering the range of Re=10–160 with $5<L_e/H<65$ for the proposed microfluidic fuel cells that integrate SGMs (N1 and N2 designs), including the cases with the reduced electrode width, i.e., W_e/H=0.25. In addition, cases of the grooveless microfluidic fuel cell (N3 design) are also provided in Fig. 5 as the limiting cases of the secondary flow being infinitely weak and the entrance length $L_{ent}\to\infty$.

3.2 Flow pattern

In the laminar flow regime, the pressure driven flow through the rectangular channel is a uniaxial Poiseuille flow. When slanted grooves are incorporated in the channel (Fig. 1), the transverse secondary flow will be generated because the fluids near the grooves are inclined in the direction along the grooves owing to the smaller flow resistance (Kjeang et al., 2007b, 2007c), which is observed in the numerical modelling results of the proposed microfluidic fuel cells that integrate SGMs. The flow pattern is shown in Fig. 6 and is the same for the N1 and N2 designs because they have identical channel geometries (the thickness of the electrodes is regarded as negligible in the numerical model).

As shown in Figs. 6a–6d, an anticlockwise helical flow pattern forms in the fuel stream, whereas a clockwise helical flow pattern forms in the oxidant stream. The provided contours of the velocity components are at positions adjacent to the 10th groove but are representative of the flow pattern in the entire channel because the velocity profile varies periodically from one groove to another approximately starting from the second groove. From the streamlines shown in Fig. 6e, it is observed that the helical flow pattern is

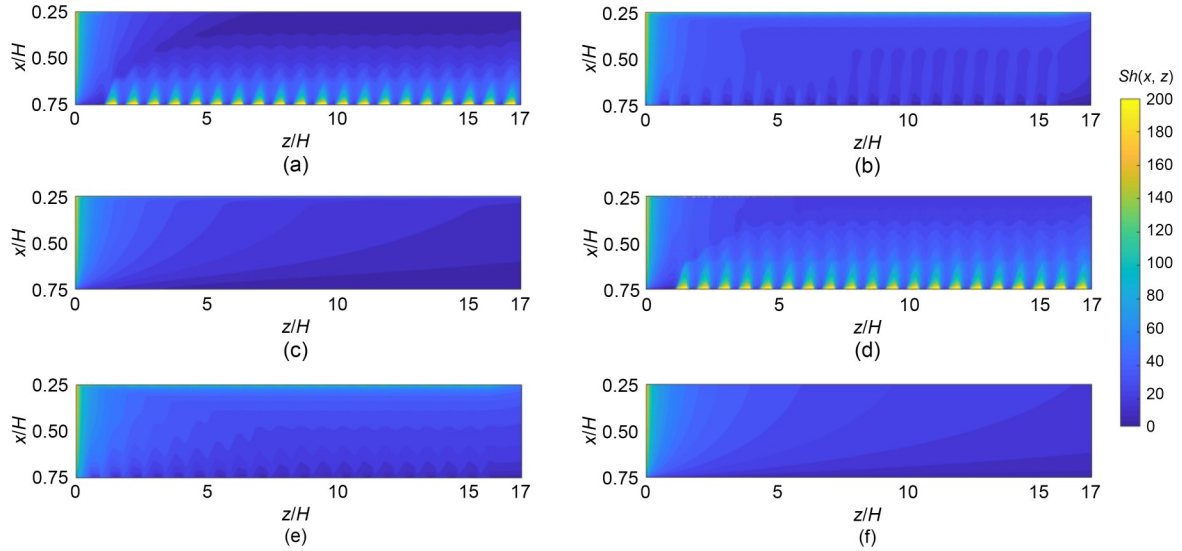

Fig. 4 Local Sherwood number distributions: (a and d), (b and e), and (c and f) are plotted for the N1, N2, and N3 designs, respectively, with (a–c) obtained by using the numerical model, whereas (d–f) is obtained by using the simplified mass transfer model at L_e/H=17 and Re=20 (plotted not to scale). Coordinate systems used in this figure are illustrated in Fig. 1

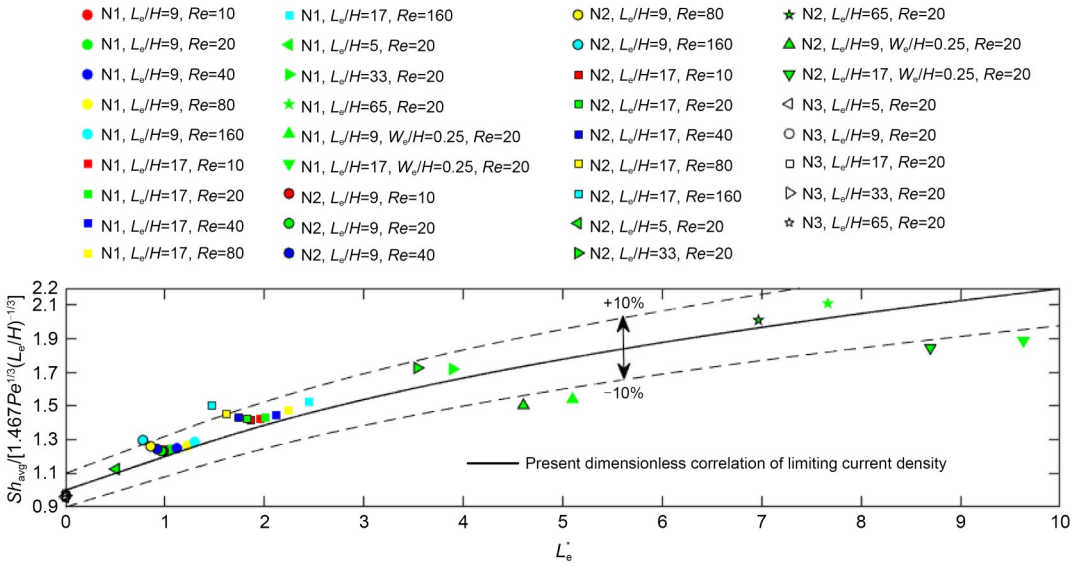

Fig. 5 Comparisons of the predictions of limiting current densities between the dimensionless correlation and numerical models. The markers represent the numerical modeling results of the N1, N2, and N3 designs with varying parameters (W_e/H=0.5 is applied where this parameter is not provided). The solid line indicates the predictions of the dimensionless correlation given by Eq. (24)

initiated near the grooves, where the electrolytes experience a rigorous upward transport through the grooves. The helical flow pattern is expected to enhance the mass transfer performance of the microfluidic fuel cell by facilitating the convective transport from the electrolyte bulk to the electrode surface (Yoon et al., 2006).

Furthermore, a unique characteristic of the helical flow pattern is that the magnitude of the transverse flow component ($v_{xy}=(v_x^2+v_y^2)^{1/2}$) decreases sharply with increasing distance from the side walls of the channel, as shown in Figs. 6a and 6b. To be specific, the maximum value of v_{xy} inside the grooves (i.e., at −190 μm< x<−150 μm and 150 μm<x<190 μm according to the set geometry, as shown in Fig. 1 and Section 2.1) is 0.15U, while the maximum v_{xy} in the gap region between the electrodes (−50 μm<x<50 μm) is merely 0.03U.

3.3 Performance of the microfluidic fuel cell

For microfluidic fuel cells that integrate groove micro-mixers, the main challenge is to enhance mass transfer of the reactants to the electrode and to simultaneously suppress convective mixing between the electrolytes (Marschewski et al., 2015). In this section, the investigation of the performance of the proposed microfluidic fuel cells that integrate SGMs is discussed by using the numerical model from the above two aspects.

First, mixing between the electrolytes when no reactions occur is investigated. Electrochemical reactions are excluded for the present to facilitate the observation of the mixing pattern (Kjeang et al., 2008), and the resulting concentration distributions of Fe^{2+} for the N1, N2, and N3 designs with L_e/H=65 at Re=20 are shown in Fig. 7. Note that the numerical modeling results of the mixing pattern are the same for the N1 and N2 designs as they have identical channel geometries. It is found that the extent of the mixing regions in the N1 and N2 designs is greater than that in the N3 design near the bottom wall of the channel, and thinner than that in the N3 design near the top wall of the channel. This phenomenon indicates convective mixing between the electrolytes in the microfluidic fuel cells that integrate SGMs. As shown in Fig. 6, a clockwise helical flow pattern forms in the oxidant stream in the N1 and N2 designs, promoting the development of the mixing region near the bottom and suppressing the development of the mixing region near the top wall. However, the convective mixing is well controlled in terms of delaying the occurrence of fuel crossover. In the N2 design, the concentration of Fe^{2+} at the cathode (embedded in the bottom wall of the channel) (Fig. 1) is not noticeable at z/H<32.52 and is approximately 2% of c_0 at z/H=40.52. In the N1 design, the concentration of Fe^{2+} at the cathode (embedded in

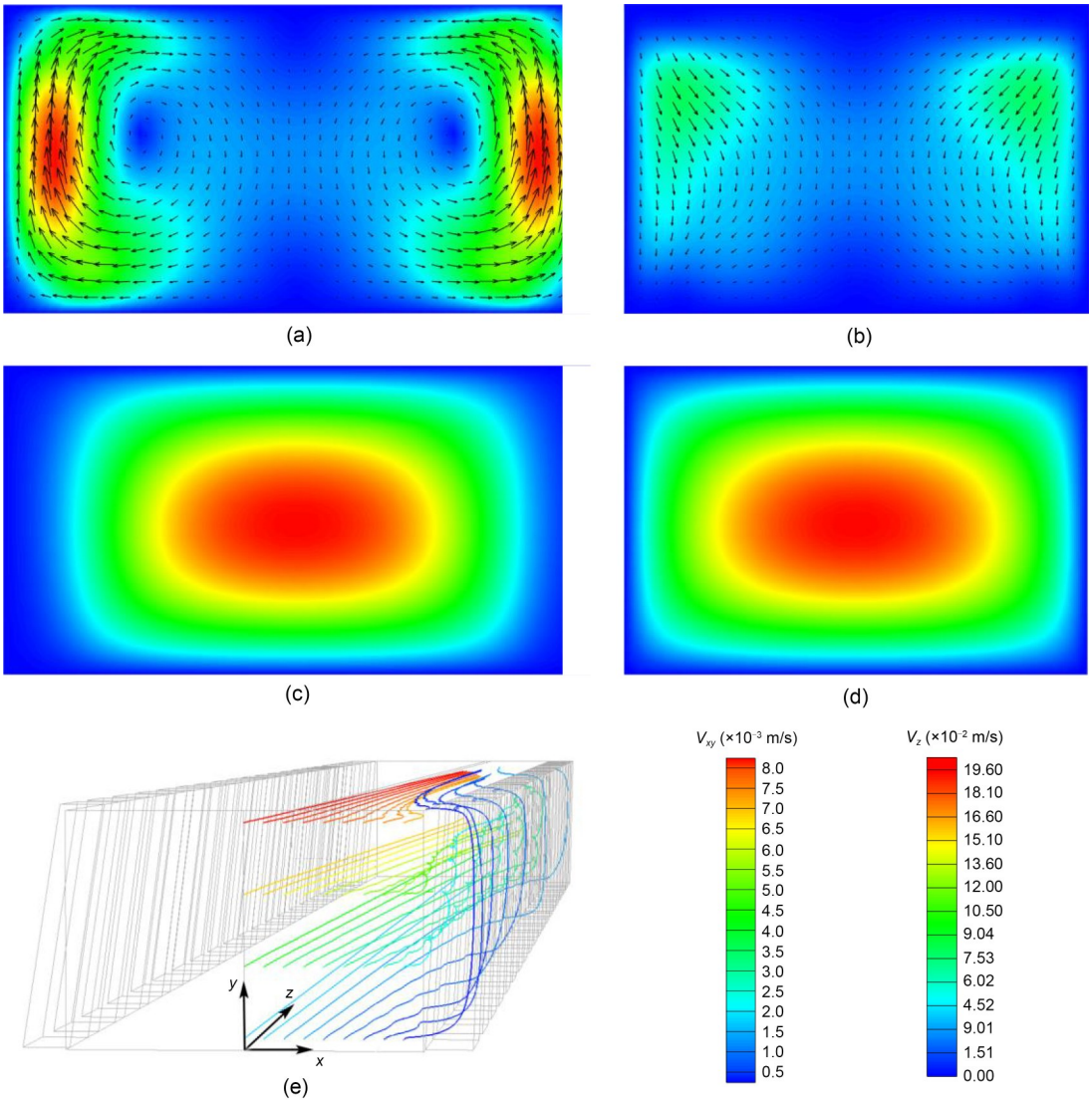

Fig. 6 Numerical modeling results of the flow patterns in the N1 and N2 designs at L_c/H=17 and Re=20: (a) and (c) are respectively the contours of the transverse flow component v_{xy} and the longitudinal flow component v_z in the cross-section through the centerline of the groove and inclined at 45° with respect to the channel; (b) and (d) are respectively the contours of v_{xy} and v_z in the cross-section through the centerline of a ridge and inclined at 45° with respect to the channel; (e) provides the streamlines on the right side of the channel

the top wall of the channel) (Fig. 1) does not increase until approximately z/H=48.75 and is approximately 3% of c_0 at z/H=56.88. Therefore, the convective mixing in the microfluidic fuel cell that integrates SGMs is well controlled, which is attributed to the relatively weak transverse secondary flow near the interface.

In addition, the operation of the microfluidic fuel cells under the mass transfer limited regime is numerically modeled to investigate the mass transfer enhancement achieved in the microfluidic fuel cells that integrate SGMs. The limiting current densities of the N1, N2, and N3 designs with varying lengths of the electrode at Re=20 are shown in Table 1. For cases with equal lengths of the electrodes, the resulting limiting current densities in the N1 and N2 designs are close to each other and are both higher than that in the N3 design. Compared to the grooveless design, the highest increment of the limiting current density by integrating SGMs into the microfluidic fuel cells is 115%, which is achieved by using the N1 design with L_c/H=65. Therefore, a significant mass transfer enhancement is achieved for the proposed microfluidic fuel cells that integrate SGMs, and the mechanism is illuminated by the discussion in the next section. Besides, to help

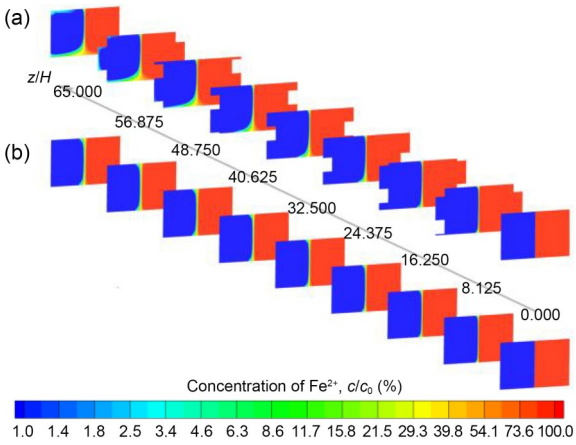

Fig. 7 Numerical modeling results of the mixing between the electrolytes when no reaction occurs at L_e/H=65 and Re=20: concentration distribution of Fe^{2+} normalized using the initial value when no reaction occurs at the electrodes, with (a) and (b) plotted for the microfluidic fuel cell integrating SGMs (N1 and N2 designs) and the grooveless microfluidic fuel cell (N3 design), respectively

Table 1 Numerical modeling results of the limiting current density in the N1, N2, and N3 designs with varying lengths of the electrode at Re=20

L_e/H	Limiting current density (A/m^2)		
	N1	N2	N3
5	27.21	27.23	23.26
9	24.69	24.54	19.12
17	23.06	22.89	15.57
33	22.19	22.29	12.50
65	21.72	20.70	10.09

readers to compare the performance of our microfluidic fuel cells with other designs, we have used the data from a related study (Marschewski et al., 2017) to create a table for that purpose (Table S1 in the electronic supplementary materials (ESM)).

3.4 Development of the depletion boundary layer

First, the numerical modeling results for the development of the depletion boundary layer of the fuel stream along the channel are presented. The thickness of the depletion boundary layer $\delta(z)$ is defined as:

$$D\frac{c_0-c_s}{\delta(z)}=\frac{1}{W_e}\int D\left(\frac{\partial c}{\partial \boldsymbol{n}}\right)_s \mathrm{d}x, \tag{26}$$

where $c_s \to 0$ under the assumption of the limiting current density regime, $\boldsymbol{n}$ represents the normal vector of the electrode pointing inside the fuel stream, and the integral on the right side of the equation is performed over the width of the electrode. The numerical modeling results of $\delta(z)$ for the N1, N2, and N3 designs with L_e/H=65 at Re=20 are shown in Fig. 8a. While the depletion boundary grows constantly along the channel in the N3 design, the growth of the depletion boundary layer in the N1 and N2 designs is terminated at a short distance from the channel, i.e., $z/H \approx 10$, and the thickness of the depletion boundary layer remains constant for a larger z/H, although periodic fluctuations occur due to the disturbance of the grooves. Because smaller thicknesses of the depletion boundary layer indicate larger concentration gradients at the electrode, the mass transfer enhancement observed in the microfluidic fuel cells that integrate SGMs (Table 1 and Section 3.3) is thus explained.

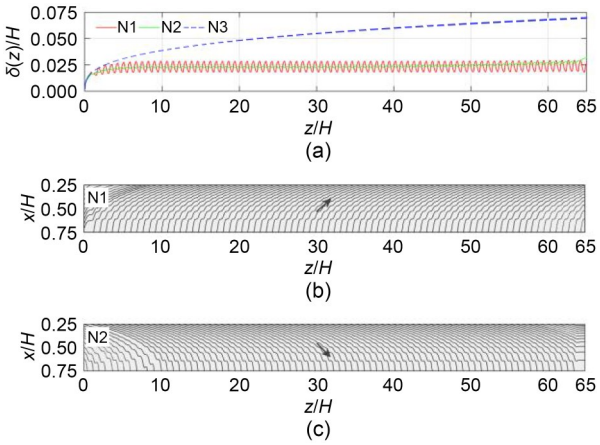

Fig. 8 Development of the depletion boundary layer along the channel at L_e/H=65 and Re=20: numerical model results of the thickness of the depletion boundary layer, $\delta(z)$, of the fuel stream for the N1, N2, and N3 designs (a); illustrations of local flow directions near the anode for the N1 (b) and N2 (c) designs based on the numerical modeling results of the velocity shear rate at the anode

In addition, the different patterns of development of the depletion boundary layer in the microfluidic fuel cells that integrate SGMs and the grooveless microfluidic fuel cell are explained by using the simplified mass transfer model described in Section 2.3. Similar to the definition of the thickness of the depletion boundary layer, $\delta(z)$, the local thickness of the depletion boundary layer, δ_{loc}, is defined as:

$$D\frac{c_0-c_s}{\delta_{loc}}=D\left(\frac{\partial c}{\partial \boldsymbol{n}}\right)_s, \tag{27}$$

where $c_s \to 0$ considering instantaneous reaction at the anode. Substituting the expression of the concentration distribution given by the simplified mass transfer model (Eq. (13)) into Eq. (27) yields:

$$\delta_{\mathrm{loc}}(s)=\Gamma\left(\frac{4}{3}\right)\frac{\left(9D\int_0^s\sqrt{\dot{\gamma}(\eta)}\ \mathrm{d}\eta\right)^{\frac{1}{3}}}{\sqrt{\dot{\gamma}(s)}}. \tag{28}$$

The s-axis is set along the local flow direction near the anode (the direction of the velocity shear rate) and s=0 where the flow enters the anode region.

For the N3 design, the flow direction near the anode is parallel to the channel, and thus the s-axis is along the channel and s=0 at the leading edge of the electrode (z=0, Fig. 1). For the N1 and N2 designs, the flow direction near the anode is inclined with respect to the channel and s-axis is set along the curves shown in Fig. 8b, which indicate the local flow directions near the anode. For the N1 design, s=0 at the leading edge of the anode (z=0), and at the right edge of the anode (x=150 μm, x/H=0.75, Fig. 1); however, in the N2 design, s=0 at the leading edge of the anode (z=0), and at the left edge of the anode (x=50 μm, x/H= 0.25, Fig. 1).

Recognizing that the qualitative feature of the relationship between δ_{loc} and s does not change under the assumption of the velocity shear rate being constant over the electrode, Eq. (28) is simplified as:

$$\delta_{\mathrm{loc}}(s)=\Gamma\left(\frac{4}{3}\right)\left(\frac{9D}{\dot{\gamma}}s\right)^{\frac{1}{3}}, \tag{29}$$

which clearly shows that the thickness of the depletion boundary layer grows along the local flow direction near the anode according to $\delta_{\mathrm{loc}}\sim s^{1/3}$.

For the grooveless microfluidic fuel cell (N3 design), Eq. (29) indicates that thickness of the depletion boundary layer grows constantly along the channel. For the microfluidic fuel cells that integrate SGMs (N1 and N2 designs), referring to Fig. 8b, growth of δ_{loc} starts where the flow enters the electrode region (s=0), progresses along the local direction of the flow near the electrode, and finally gets arrested where the flow exits from the electrode region. Referring to Fig. 8b, the thickness of the depletion boundary layer is repetitive along the channel for the major part of the electrode, where the flow enters the electrode region from the side edge of the electrode. The termination of the growth of the thickness of the depletion boundary layer along the channel (Fig. 8a) is thus explained.

Besides, as shown in Fig. 8a, the thickness of the depletion boundary layer in the N2 design regrows slowly from $z/H\approx40$, which is attributed to the reduced concentration of the reactant (Fe^{2+}) near the anode due to mixing between the electrolytes. In contrast, such regrowth of the depletion boundary layer is negligible in the N1 design, because the influence of convective mixing on the electrode region is less prominent in the N1 design than in the N2 design (Fig. 7 and Section 3.3).

3.5 Effects of design parameters on limiting current density

Given the distinct patterns of the development of the depletion boundary layer along the channel in the microfluidic fuel cells that integrate SGMs (Section 3.4), the effects of the design parameters of the microfluidic fuel cell on the limiting current density can be fundamentally different from those in the grooveless microfluidic fuel cell. In this section, a parametric study is described that is based on the dimensionless correlations of the limiting current density (Eq. (24)) derived via the simplified mass transfer model.

To highlight the effects of the design parameters, Eq. (24) is rewritten in the following form:

$$\frac{Sh_{\mathrm{avg}}}{1.467Pe^{\frac{1}{3}}}=\begin{cases}0.2\left(\dfrac{L_{\mathrm{e}}}{H}\right)^{\frac{2}{3}}\left(\dfrac{L_{\mathrm{ent}}}{H}\right)^{-1}+\left(\dfrac{L_{\mathrm{e}}}{H}\right)^{-\frac{1}{3}}, & L_{\mathrm{e}}\leqslant L_{\mathrm{ent}},\\ 0.2\left(\dfrac{L_{\mathrm{ent}}}{H}\right)^{\frac{2}{3}}\left(\dfrac{L_{\mathrm{e}}}{H}\right)^{-1}+\left(\dfrac{L_{\mathrm{ent}}}{H}\right)^{-\frac{1}{3}}, & L_{\mathrm{e}}>L_{\mathrm{ent}}.\end{cases} \tag{30}$$

As shown in Fig. 5, the above equation can be applied to both the N1 and N2 designs and in two cases, i.e., the length of the electrode that is smaller than or larger than the entrance length. In addition, Eq. (30) can also be applied to the N3 design by considering the limit $L_{\mathrm{ent}}\to\infty$. The characteristic parameters are L_e/H (i.e., the dimensionless length of the electrode) and L_{ent}/H (i.e., the dimensionless entrance length). It should be noted that the parameter L_{ent}/H incorporates the comprehensive effects of the width and position of the electrode, the aspect ratio of the cross section

of the channel, and the geometric parameters of the slanted grooves that are incorporated on the side walls of the channel. Additionally, the parameter L_{ent}/H is independent of the parameter L_e/H (according to the definition of the entrance length L_{ent} in Section 2.3.3) and is approximately independent of the Reynolds number (Fig. 5). Considering that the validation of the developed dimensionless correlation (Eq. (24)) is based on the parameter range of $5<L_e/H<65$ and $1.8<L_{ent}/H<11.6$, a parametric study is conducted for the characteristic parameters in the range of $5<L_e/H<65$ and $2<L_{ent}/H<10$, and the results are shown in Fig. 9. Nevertheless, the main findings can also be extended to cases with smaller L_{ent}/H, because the entrance length L_{ent} decreases with increasing magnitude of the transverse flow component (refer to the definition of L_{ent} in Section 2.3.3), and increased magnitude of the transverse flow component can be achieved without changes in the overall helical flow pattern (Lynn and Dandy, 2007). For comparison, the benchmark for Sh_{avg} of the grooveless microfluidic fuel cell (i.e., $L_{ent}/H\to\infty$) is also provided.

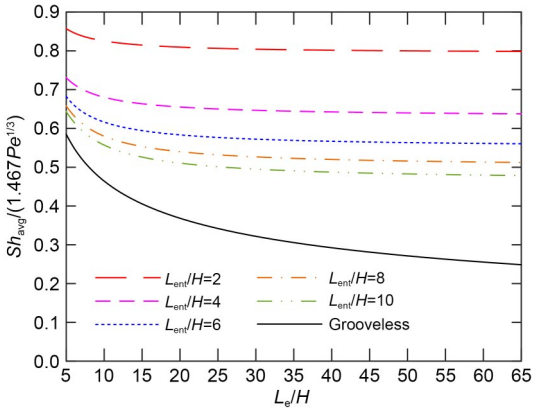

Fig. 9 Effects of the design parameters on the limiting current density as predicted by the dimensionless correlation (Eq. (30))

As shown in Fig. 9, with increasing length of the electrode the limiting current density deceases drastically in the grooveless microfluidic fuel (consistent with the previous findings (Kirtland et al., 2006)), but it is an asymptotic value for the microfluidic fuel cells with integrated SGMs. Referring to Eq. (30), the asymptotic value of the limiting current density is given by:

$$Sh_\infty = 1.467\left(\frac{Pe}{L_{ent}/H}\right)^{\frac{1}{3}}. \tag{31}$$

Therefore, with the integration of SGMs, the limiting current density becomes less sensitive to the length of the electrode, and a longer electrode can be used to achieve higher fuel utilization while maintaining a high limiting current density. Taking the case of L_{ent}/H=2 as an example, the limiting current density decreases by no more than 4% when the electrode length increases from L_{ent}/H=10 to 60 (corresponding to an increase in the fuel utilization of over 480%).

In addition, it is shown in Fig. 9 that the limiting current density increases significantly with deceasing entrance length L_{ent}. This can also be seen from Eq. (31), which shows that the asymptotic value of the limiting current density Sh_∞ increases with deceasing entrance length L_{ent}. Referring to the definition of L_{ent} in Section 2.3.3, L_{ent} is negatively dependent on the relative magnitude of the transverse flow component with that of the main flow and is positively dependent on the width of the electrode. Therefore, the limiting current density increases significantly with increasing magnitude of the transverse flow near the electrode and the reduced width of the electrode. Note, however, that the microfluidic fuel cell design should be optimized with other design considerations, such as convective mixing between the electrolytes (Yoon et al., 2006), ohmic losses, and pumping energy through the channel (Shaegh et al., 2011).

While it is convenient to conduct parametric studies using the developed dimensionless correlations of limiting current density, the application of the equation for predicting the limiting current density corresponding to given channel design remains challenging, because the estimation of the entrance length is required. A brief discussion of a method for approximating the entrance length is presented below. First, the influence of the slanted grooves on the fluid flow can be substituted by an effective slip boundary condition at the side wall of the channel, and the magnitude of the slip velocity can be calculated by using an established correlation between the slip velocity and the geometric parameters of the groove channel (Stroock et al., 2002). The 3D flow in the channel is then approximated by the superposition of the unperturbed Poiseuille flow and the 2D transverse flow in the cross-section of the channel (Stroock and Mcgraw, 2004). Under the Stokes approximation, the transverse flow can be solved analytically. Finally, the obtained velocity profile can be used to calculate the entrance length (Section 2.3.3).

3.6 Future work

Recognizing the importance and the potential impacts of the proposed design on the medium consumption and response time, we will investigate these issues in greater depth in our future study, and this will lead us to more interesting findings and conclusions. Additionally, the present study was mainly focused on numerical simulation and aimed at in-depth understanding of the mechanism of the groove micro-mixers design. In our future study, we plan to perform more comprehensive experimental studies, including cyclic voltammetry and electrochemical impedance spectroscopy tests, to further investigate the performance of microfluidic fuel cells.

4 Conclusions

Microfluidic fuel cells that integrate SGMs on the side walls of the channel have been proposed and studied. First, a significant mass transfer enhancement is achieved and the limiting current density is increased by as much as 115% compared to the grooveless microfluidic fuel cell. Furthermore, convective mixing between the electrolytes is well controlled owing to the weak transverse secondary flow near the interface between the electrolytes.

Second, the development of the depletion boundary layer along the channel in the proposed microfluidic fuel cells that integrate SGMs is found to display a distinct pattern compared to that in the grooveless microfluidic fuel cell. The growth of the thickness of the depletion boundary layer is terminated at about $10H$ from the channel entrance. The different patterns in the designs that integrate SGMs and the grooveless design are explained by using a simplified mass transfer model. The thickness of the depletion boundary layer grows along the local flow direction near the electrode approximately according to $\delta_{loc}\sim s^{1/3}$ in both types of microfluidic fuel cells, but the local flow direction near the electrode is inclined with respect to the channel instead of being parallel to the channel in the microfluidic fuel cells that integrate SGMs.

Lastly, the analysis of the effects of the design parameters by using the developed dimensionless correlations reveals that the limiting current density has an asymptotic value with increasing length of the electrode and is significantly influenced by the magnitude of the transverse flow component near the electrode and by the width of the electrode.

Acknowledgments

This work is supported by the National Natural Science Foundation of China (No. 51606164).

Author contributions

Jinchi SUN designed the research and derived the analytical models. Xiongwei TIAN and Zhangqing LIU performed the simulation and data processing. Menglian ZHENG supervised the research. Jinchi SUN, Xiongwei TIAN, and Zhangqing LIU wrote the first draft of the manuscript. Menglian ZHENG and Jie SUN revised and edited the final version.

Conflict of interest

Jinchi SUN, Xiongwei TIAN, Zhangqing LIU, Jie SUN, and Menglian ZHENG declare that they have no conflict of interest.

References

Ahmed DH, Park HB, Sung HJ, 2008. Optimum geometrical design for improved fuel utilization in membraneless micro fuel cell. *Journal of Power Sources*, 185(1):143-152. https://doi.org/10.1016/j.jpowsour.2008.06.045

Bazylak A, Sinton D, Djilali N, 2005. Improved fuel utilization in microfluidic fuel cells: a computational study. *Journal of Power Sources*, 143(1-2):57-66. https://doi.org/10.1016/j.jpowsour.2004.11.029

Brushett FR, Jayashree RS, Zhou WP, et al., 2009. Investigation of fuel and media flexible laminar flow-based fuel cells. *Electrochimica Acta*, 54(27):7099-7105. https://doi.org/10.1016/j.electacta.2009.07.011

Chang MH, Chen FL, Fang NS, 2006. Analysis of membraneless fuel cell using laminar flow in a Y-shaped microchannel. *Journal of Power Sources*, 159(2):810-816. https://doi.org/10.1016/j.jpowsour.2005.11.066

Choban ER, Markoski LJ, Wieckowski A, et al., 2004. Microfluidic fuel cell based on laminar flow. *Journal of Power Sources*, 128(1):54-60. https://doi.org/10.1016/j.jpowsour.2003.11.052

Choban ER, Waszczuk P, Kenis PJA, 2005a. Characterization of limiting factors in laminar flow-based membraneless microfuel cells. *Electrochemical and Solid-State Letters*, 8(7):A348. https://doi.org/10.1149/1.1921131

Choban ER, Spendelow JS, Gancs L, et al., 2005b. Membraneless laminar flow-based micro fuel cells operating in alkaline, acidic, and acidic/alkaline media. *Electrochimica Acta*, 50(27):5390-5398. https://doi.org/10.1016/j.electacta.2005.03.019

Cohen JL, Volpe DJ, Westly DA, et al., 2005a. A dual electrolyte H_2/O_2 planar membraneless microchannel fuel cell system with open circuit potentials in excess of 1.4 V. *Langmuir*, 21(8):3544-3550.

https://doi.org/10.1021/la0479307

Cohen JL, Westly DA, Pechenik A, 2005b. Fabrication and preliminary testing of a planar membraneless microchannel fuel cell. *Journal of Power Sources*, 139(1-2):96-105. https://doi.org/10.1016/j.jpowsour.2004.06.072

da Mota N, Finkelstein DA, Kirtland JD, et al., 2012. Membraneless, room-temperature, direct borohydride/cerium fuel cell with power density of over 0.25 W/cm^2. *Journal of the American Chemical Society*, 134(14):6076-6079. https://doi.org/10.1021/ja211751k

Dyer CK, 2002. Fuel cells for portable applications. *Journal of Power Sources*, 106(1-2):31-34. https://doi.org/10.1016/S0378-7753(01)01069-2

Ferrigno R, Stroock AD, Clark TD, et al., 2002. Membraneless vanadium redox fuel cell using laminar flow. *Journal of the American Chemical Society*, 124(44):12930-12931. https://doi.org/10.1021/ja020812q

Forbes TP, Kralj JG, 2012. Engineering and analysis of surface interactions in a microfluidic herringbone micromixer. *Lab on a Chip*, 12(15):2634-2637. https://doi.org/10.1039/c2lc40356k

Gurrola MP, Escalona-Villalpando RA, Arjona N, et al., 2021. Microfluidic fuel cells. *In*: Encyclopedia of Electrochemistry. Wiley. https://doi.org/10.1002/9783527610426.bard120075

Ha SM, Ahn Y, 2014. Laminar flow-based micro fuel cell utilizing grooved electrode surface. *Journal of Power Sources*, 267:731-738. https://doi.org/10.1016/j.jpowsour.2014.06.005

Hasegawa S, Shimotani K, Kishi K, et al., 2005. Electricity generation from decomposition of hydrogen peroxide. *Electrochemical and Solid-State Letters*, 8(2):A119-A121. https://doi.org/10.1149/1.1849112

Jayashree RS, Gancs L, Choban ER, et al., 2005. Air-breathing laminar flow-based microfluidic fuel cell. *Journal of the American Chemical Society*, 127(48):16758-16759. https://doi.org/10.1021/ja054599k

Jayashree RS, Egas D, Spendelow JS, et al., 2006. Air-breathing laminar flow-based direct methanol fuel cell with alkaline electrolyte. *Electrochemical and Solid-State Letters*, 9(5):A252. https://doi.org/10.1149/1.2185836

Jayashree RS, Yoon SK, Brushett FR, et al., 2010. On the performance of membraneless laminar flow-based fuel cells. *Journal of Power Sources*, 195(11):3569-3578. https://doi.org/10.1016/j.jpowsour.2009.12.029

Kirtland JD, McGraw GJ, Stroock AD, 2006. Mass transfer to reactive boundaries from steady three-dimensional flows in microchannels. *Physics of Fluids*, 18(7):073602. https://doi.org/10.1063/1.2222389

Kirtland JD, Siegel CR, Stroock AD, 2009. Interfacial mass transport in steady three-dimensional flows in microchannels. *New Journal of Physics*, 11(7):075028. https://doi.org/10.1088/1367-2630/11/7/075028

Kjeang E, Proctor BT, Brolo AG, et al., 2007a. High-performance microfluidic vanadium redox fuel cell. *Electrochimica Acta*, 52(15):4942-4946. https://doi.org/10.1016/j.electacta.2007.01.062

Kjeang E, Roesch B, McKechnie J, et al., 2007b. Integrated electrochemical velocimetry for microfluidic devices. *Microfluidics and Nanofluidics*, 3(4):403-416. https://doi.org/10.1007/s10404-006-0128-1

Kjeang E, McKechnie J, Sinton D, et al., 2007c. Planar and three-dimensional microfluidic fuel cell architectures based on graphite rod electrodes. *Journal of Power Sources*, 168(2):379-390. https://doi.org/10.1016/j.jpowsour.2007.02.087

Kjeang E, Michel R, Harrington DA, et al., 2008. A microfluidic fuel cell with flow-through porous electrodes. *Journal of the American Chemical Society*, 130(12):4000-4006. https://doi.org/10.1021/ja078248c

Kjeang E, Djilali N, Sinton D, 2009. Microfluidic fuel cells: a review. *Journal of Power Sources*, 186(2):353-369. https://doi.org/10.1016/j.jpowsour.2008.10.011

Kundu A, Jang JH, Gil JH, et al., 2007. Micro-fuel cells—current development and applications. *Journal of Power Sources*, 170(1):67-78. https://doi.org/10.1016/j.jpowsour.2007.03.066

Lee J, Lim KG, Palmore GTR, et al., 2007. Optimization of microfluidic fuel cells using transport principles. *Analytical Chemistry*, 79(19):7301-7307. https://doi.org/10.1021/ac070812e

Lee JW, Kjeang E, 2013. Nanofluidic fuel cell. *Journal of Power Sources*, 242:472-477. https://doi.org/10.1016/j.jpowsour.2013.05.129

Lee SW, Ahn Y, 2015. Influence of electrode groove geometry on the passive control of the depletion layer in microfluidic fuel cells. *Journal of Micromechanics and Microengineering*, 25(12):127001. https://doi.org/10.1088/0960-1317/25/12/127001

Lynn NS, Dandy DS, 2007. Geometrical optimization of helical flow in grooved micromixers. *Lab on a Chip*, 7(5):580-587. https://doi.org/10.1039/b700811b

Marschewski J, Jung S, Ruch P, et al., 2015. Mixing with herringbone-inspired microstructures: overcoming the diffusion limit in co-laminar microfluidic devices. *Lab on a Chip*, 15(8):1923-1933. https://doi.org/10.1039/C5LC00045A

Marschewski J, Ruch P, Ebejer N, et al., 2017. On the mass transfer performance enhancement of membraneless redox flow cells with mixing promoters. *International Journal of Heat and Mass Transfer*, 106:884-894. https://doi.org/10.1016/j.ijheatmasstransfer.2016.10.030

Modestino MA, Fernandez Rivas D, Hashemi SMH, et al., 2016. The potential for microfluidics in electrochemical energy systems. *Energy & Environmental Science*, 9(11):3381-3391. https://doi.org/10.1039/C6EE01884J

Moreno-Zuria A, Ortiz-Ortega E, Gurrola MP, et al., 2017. Evolution of microfluidic fuel stack design as an innovative alternative to energy production. *International Journal of Hydrogen Energy*, 42(46):27929-27939. https://doi.org/10.1016/j.ijhydene.2017.05.185

Nasharudin MN, Kamarudin SK, Hasran UA, et al., 2014. Mass transfer and performance of membrane-less micro

fuel cell: a review. *International Journal of Hydrogen Energy*, 39(2):1039-1055. https://doi.org/10.1016/j.ijhydene.2013.09.135

Newman J, 1968. Engineering design of electrochemical systems. *Industrial and Engineering Chemistry*, 60(4):12-27. https://doi.org/10.1021/ie50700a005

Nguyen NT, Chan SH, 2006. Micromachined polymer electrolyte membrane and direct methanol fuel cells—a review. *Journal of Micromechanics and Microengineering*, 16(4): R1-R12. https://doi.org/10.1088/0960-1317/16/4/R01

Shaegh SAM, Nguyen NT, Chan SH, 2011. A review on membraneless laminar flow-based fuel cells. *International Journal of Hydrogen Energy*, 36(9):5675-5694. https://doi.org/10.1016/j.ijhydene.2011.01.063

Shaegh SAM, Nguyen NT, Chan SH, et al., 2012. Air-breathing membraneless laminar flow-based fuel cell with flow-through anode. *International Journal of Hydrogen Energy*, 37(4):3466-3476. https://doi.org/10.1016/j.ijhydene.2011.11.051

Stroock AD, Mcgraw GJ, 2004. Investigation of the staggered herringbone mixer with a simple analytical model. *Philosophical Transactions of the Royal Society of A: Mathematical, Physical and Engineering Sciences*, 362(1818): 971-986. https://doi.org/10.1098/rsta.2003.1357

Stroock AD, Dertinger SK, Whitesides GM, et al., 2002. Patterning flows using grooved surfaces. *Analytical Chemistry*, 74(20):5306-5312. https://doi.org/10.1021/ac0257389

Tsuchiya H, Kobayashi O, 2004. Mass production cost of PEM fuel cell by learning curve. *International Journal of Hydrogen Energy*, 29(10):985-990. https://doi.org/10.1016/j.ijhydene.2003.10.011

Xuan J, Leung DYC, Leung MKH, et al., 2011. Chaotic flow-based fuel cell built on counter-flow microfluidic network: predicting the over-limiting current behavior. *Journal of Power Sources*, 196(22):9391-9397. https://doi.org/10.1016/j.jpowsour.2011.06.065

Yoon SK, Fichtl GW, Kenis PJA, 2006. Active control of the depletion boundary layers in microfluidic electrochemical reactors. *Lab on a Chip*, 6(12):1516-1524. https://doi.org/10.1039/b609289f

Electronic supplementary materials

Table S1